

# Metabolic Regulatory Network Kinetic Modeling with Multiple Isotopic Tracers for iPSCs

Wei Xie<sup>1</sup>, Keqi Wang<sup>1</sup>, and Sarah Harcum<sup>2</sup>

<sup>1</sup>Northeastern University

<sup>2</sup>Clemson University

August 7, 2023

## Abstract

The rapidly expanding market for regenerative medicines and cell therapies highlights the need to advance the understanding of cellular metabolisms and improve the prediction of cultivation production process for human induced pluripotent stem cells (iPSCs). In this paper, a metabolic kinetic model was developed to characterize underlying mechanisms of iPSC culture process, which can predict cell response to environmental perturbation and support process control. This model focuses on the central carbon metabolic network, including glycolysis, pentose phosphate pathway (PPP), tricarboxylic acid (TCA) cycle, and amino acid metabolism, which plays a crucial role to support iPSC proliferation. Heterogeneous measures of extracellular metabolites and multiple isotopic tracers collected under multiple conditions were used to learn metabolic regulatory mechanisms. Systematic cross-validation confirmed the model's performance in terms of providing reliable predictions on cellular metabolism and culture process dynamics under various culture conditions. Thus, the developed mechanistic kinetic model can support process control strategies to strategically select optimal cell culture conditions at different times, ensure cell product functionality, and facilitate large-scale manufacturing of regenerative medicines and cell therapies.

**BIOTECHNOLOGY & BIOENGINEERING**

# Metabolic Regulatory Network Kinetic Modeling with Multiple Isotopic Tracers for iPSCs

Keqi Wang<sup>1</sup> | Wei Xie <sup>\*,1</sup> | Sarah W. Harcum <sup>†,2</sup>

<sup>1</sup>Department of Mechanical and Industrial Engineering, Northeastern University, Boston, MA 02115, USA

<sup>2</sup>Department of Bioengineering, Clemson University, Clemson, SC, USA

**Correspondence**

\*Department of Mechanical and Industrial Engineering, Northeastern University, Boston, MA 02115, USA.

Email: w.xie@northeastern.edu

†Department of Bioengineering, Clemson University, Clemson, SC, USA.

Email: harcum@clemson.edu

**Abstract**

The rapidly expanding market for regenerative medicines and cell therapies highlights the need to advance the understanding of cellular metabolisms and improve the prediction of cultivation production process for human induced pluripotent stem cells (iPSCs). In this paper, a metabolic kinetic model was developed to characterize underlying mechanisms of iPSC culture process, which can predict cell response to environmental perturbation and support process control. This model focuses on the central carbon metabolic network, including glycolysis, pentose phosphate pathway (PPP), tricarboxylic acid (TCA) cycle, and amino acid metabolism, which plays a crucial role to support iPSC proliferation. Heterogeneous measures of extracellular metabolites and multiple isotopic tracers collected under multiple conditions were used to learn metabolic regulatory mechanisms. Systematic cross-validation confirmed the model's performance in terms of providing reliable predictions on cellular metabolism and culture process dynamics under various culture conditions. Thus, the developed mechanistic kinetic model can support process control strategies to strategically select optimal cell culture conditions at different times, ensure cell product functionality, and facilitate large-scale manufacturing of regenerative medicines and cell therapies.

**KEYWORDS:**

Cell Therapy Manufacturing, Induced Pluripotent Stem Cells (iPSCs), Metabolic Regulatory Network, Process Dynamic Model, Stable Isotope Labeling

## 1 | INTRODUCTION

Cell therapeutics and regenerative medicines have the potential to treat and prevent diseases, such as cancers, and cardiovascular and hematologic diseases<sup>1,2</sup>. The cell therapy market is experiencing unparalleled growth and the projected worth of the relevant market is expected to be over \$8 billion in 2025<sup>3</sup>. To meet the rising demand, cost reductions in manufacturing and increases in quality for human induced pluripotent stem cells (iPSCs) on a large scale are crucial for the success of cell therapies<sup>4</sup>. Unlike traditional biopharmaceuticals, the

cells are the product with functional identity depending on the regulatory metabolic dynamic behaviors.

The efficacy of the cells is very sensitive to culture conditions. Variability in the culture conditions can lead to reduced yields and heterogeneous cell populations. Heterogeneous cell populations have been observed to increase the potential for tumor or teratoma formulation in the patient<sup>5</sup>. Traditional cell culture process control strategies often are ad hoc and rely solely on experimental approaches or PID controllers ignoring long-term effects. The optimal design and control of mammalian cell culture processes, especially iPSCs, can be laborious due to the limited understanding of cellular metabolisms and end-to-end cultivation process dynamics<sup>6,7</sup>.

In order to determine the best culture conditions, accounting for cell life cycle, relationships between culture conditions and the output trajectory (i.e., cell functional identity and yield) are needed. Mechanistic dynamics models have the capability to predict cell outcomes (e.g., metabolic flux rates), which can be used to assess product quality. These models provide systems-level descriptions of metabolic networks and regulatory mechanisms. With this complex and high-level cellular description, it is possible to interface such models with process control algorithms to strategically select the optimal culture conditions at different times.

The proposed model for the iPSC metabolic network and regulation mechanisms combines four modeling approaches to leverage the strengths of each approach: (1) metabolic flux analysis (MFA), (2) flux balance analysis (FBA), (3)  $^{13}\text{C}$ -MFA, and (4) kinetic models. In MFA, metabolic flux rates (such as substrate uptake rate and metabolite secretion rate) are estimated based on experimental measurements subject to stoichiometric constraints. Under the standard assumption of (pseudo) steady state for intracellular metabolites, the sum of all fluxes producing a metabolite is equal to the sum of all fluxes consuming that metabolite. This technique is frequently used to compare the metabolism of different cell lines to assess the activity of individual pathways under different cultivation conditions<sup>8</sup>. However, intracellular metabolites can change during cell proliferation<sup>9</sup>.

Stable isotope studies, integrating with MFA, have provided more detailed information on intracellular state and metabolic pathways, namely  $^{13}\text{C}$ -MFA can precisely estimate metabolic reaction rates. Typically these flux rates are estimated from measured intracellular mass isotopomer distribution (MID) patterns and external metabolites concentrations, which requires the assumption of isotopic and metabolic steady state<sup>10,11,12,13</sup>. Several modeling tools<sup>14,10,11</sup> can predict fluxes for cultures that have not reached isotopic and/or fluxes steady state. However, these tools are not easily integrated into the process control of iPSC cultures.

Another approach to model cell dynamics includes kinetic-metabolic models<sup>6</sup>. The vast majority of the kinetic models use Monod and Michaelis–Menten expression formalisms modeling the metabolic regulation mechanisms<sup>15,16,17,6,18</sup>. For Chinese hamster ovary (CHO) cell cultures, kinetic-metabolic models include glycolysis, pentose phosphate pathway (PPP), tricarboxylic acid (TCA) cycle, respiratory chain, as well as the regulatory functions from energy shuttles (ATP/ADP) and cofactors (NADH, NAD<sup>+</sup>, NADPH, NADP<sup>+</sup>); this high level of details is required to predict hypoxic perturbation<sup>16,17</sup>. For example, the study<sup>18</sup> proposed a Monod model that characterizes the cell flux rate response to environmental perturbation. That study used limiting substrate kinetics to calculate the extracellular metabolite consumption/production

rates and further infer metabolic flux rates built on a static MFA assumption, i.e., assuming the intracellular metabolites are at the pseudo-steady state. Even though several *in silico* metabolomic platforms have been developed for CHO cells<sup>15,16,17,6,18</sup>, a metabolic regulatory network simulator for iPSC has not been developed.

Stirred suspension cultures are often recommended for large-scale manufacturing of iPSCs<sup>19,20</sup>. Due to strong cell-cell interactions and extracellular matrix secretion, iPSCs can form large cell aggregates in suspension bioreactors, resulting in insufficient nutrient supply and extra metabolic waste build-up for the cells located at core<sup>21</sup>. This issue can be more serious as the aggregates grow. Understanding the implications of these concentration variations is crucial for the survival and proliferation of iPSCs<sup>22</sup>, and also essential for maintaining the quality assurance of cell products. Thus, the primary aim of this study is to develop and validate an iPSC metabolic regulatory network mechanistic model capable of predicting cell responses to environmental variations. In iPSC aggregate cultures, the well-established pattern involves low glucose and high lactate concentrations at the aggregate center. Considering the significance of these metabolites, this paper focuses on evaluating the effects stemming from variations in extracellular glucose and lactate concentrations, utilizing data gathered from well-designed monolayer K3 iPSC cultures<sup>4</sup>.

To support the prediction of iPSC response to environmental variations during the culture process, the proposed model primarily concentrates on central metabolism, given its pivotal role in stem cell proliferation, biosynthesis, and functionality. The developed mechanistic model characterizes time-variate reaction dynamics and regulatory mechanisms. This model used previously obtained experimentally MID for iPSC cultures to estimate model parameters. During the model development, the level of detail required for key pathways was explored, namely the PPP and branched amino acids uptake rates into the TCA cycle. The model development, validation, and final model details will be presented with comparisons to the experimental data.

The proposed model structure, comprising the metabolic reaction network and flux regulatory mechanism, can be easily customized to suit various mammalian cell culture systems, e.g., embryonic stem cells (ESCs), CHO, etc. This adaptability stems from the underlying principles and general characteristics of metabolic regulation that are common across various mammalian cells. Through the collection of extracellular metabolite concentrations and intracellular MID measurements, this mechanistic model can be adeptly employed to analyze and forecast the behavior of other mammalian cell cultures with consistent accuracy and reliability.

## 2 | DATA DESCRIPTION

Briefly, the data used to estimate the model parameters were derived from an experimental study of K3 iPSCs, where mono-layer cultures were conducted in 6-well plates and 60 mm cell culture dishes<sup>4</sup>. The data encompassed extracellular metabolite measurements and isotopic labeling details for four distinct culture conditions, utilizing three tracers: glucose, glutamine, and lactate. The four different initial culture media concentrations were: (1) high glucose and low lactate (HGLL); standard initial conditions, i.e., 18.3 mM glucose and 0 mM lactate; (2) high glucose and high lactate (HGHL), i.e., 18.3 mM glucose and 20 mM lactate; (3) low glucose and low lactate (LGLL), i.e., 5.6 mM glucose and 0 mM lactate; and (4) low glucose and high lactate (LGHL), i.e., 5.6 mM glucose and 20 mM lactate. Table 1 presents the media concentrations used for each condition, encompassing glucose, lactate, and supplemented sodium chloride concentrations. Furthermore, 2.75 mM glutamine was included in each condition. These concentrations were chosen to ensure comparable growth rates across all conditions while maintaining pluripotency<sup>4</sup>.

**TABLE 1** The media formulations for K3 iPSC cultures include initial concentrations of glucose, sodium L-lactate, and supplemented sodium chloride (NaCl). NaCl was added to balance osmolarity in cultures lacking sodium lactate. Additionally, the media contains 2.75 mM L-glutamine.

| Component  | Concentrations (mM) |      |       |      |
|------------|---------------------|------|-------|------|
|            | HGLL                | HGHL | LGLL  | LGHL |
| Glucose    | 18.3                | 18.3 | 5.6   | 5.6  |
| Lactate    | -                   | 20.0 | -     | 20.0 |
| Added NaCl | +20.0               | -    | +20.0 | -    |

Cell density, glucose, lactate, pyruvate, and extracellular amino acid concentrations were obtained for each condition at 0-, 12-, 24-, 36-, and 48-h. Intracellular amino acid MIDs are obtained from parallel labeling experiments that used [1,2-<sup>13</sup>C<sub>2</sub>] glucose, [U-<sup>13</sup>C<sub>5</sub>] L-glutamine, and [U-<sup>13</sup>C<sub>3</sub>] sodium L-lactate (when lactate was added to culture media). A schematic of the time-course measurements as shown in Figure 1 were used to develop the metabolic regulatory network kinetic model for iPSC culture process.

## 3 | MODEL DEVELOPMENT

The iPSC metabolic regulatory network kinetic model will be presented by the four levels of development. Section 3.1 provides the general dynamic model description, including

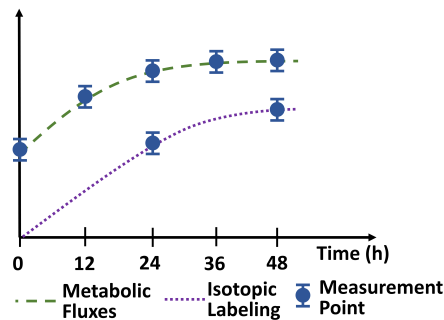


**FIGURE 1** A schematic of the time-course extracellular concentrations measurements and isotopic intracellular amino acid MIDs for the experimental iPSC cultures. Metabolites were measured every 12 h, while the MIDs were only obtained at 24- and 48-h. The 24-h MIDs were considered to be at metabolic steady-state, but not isotopic steady-state, while by 48-h, both metabolic and isotopic steady-state were reached.

(1) regulatory metabolic network kinetic modeling; and (2) time-course isotopic labeling simulation. Section 3.2 presents the iPSC metabolic reaction network which includes central carbon metabolism. In Section 3.3, metabolic flux kinetics, characterizing cell response to environmental variations, were learned from time-course extracellular concentration measurements and MIDs. Finally, in Section 3.4, the assessment of fit and validation of the dynamic model for the iPSC cultures is discussed, where the objective function and goodness-of-fit will be presented.

### 3.1 | Metabolic Network Kinetic Modeling

In this section, the general regulatory metabolic network kinetic model and time-course isotopic labeling simulation are presented. The kinetic model captures the dynamic changes in cell density, and extracellular and intracellular metabolite concentrations, where the changing rates of metabolites depend on the concentration of substrates and inhibitors. To incorporate the mass isotopic data, a dynamic isotopic labeling system was constructed, and a time-course isotopic labeling simulation was developed. Overall, the metabolic reaction network kinetic model provides a comprehensive understanding of the underlying mechanisms of the iPSC culture process.

**(1) Metabolic Reaction Network Kinetic Model.** The data from the study for K3 iPSCs were collected during the exponential growth phase<sup>4</sup>. Through experimental design and statistical analysis, our previous study<sup>4</sup> discovered uniform specific cell growth rates ( $\mu$ ) across the four batch culture conditions (HGLL, HGHL, LGLL, and LGHL), maintaining pluripotency. This suggests that glucose and lactate concentrations within these ranges did not notably influence K3 iPSC

growth rates and did not have a detrimental impact on human K3 iPSC pluripotency. Thus the classical cell density formalism was used to relate growth and the cell density, denoted by  $X(t)$  (cells/cm<sup>2</sup>), at time  $t$  as,

$$\frac{dX(t)}{dt} = \mu X(t). \quad (1)$$

The extracellular metabolite concentrations at time  $t$  are denoted by a vector with dimension  $p$ , i.e.,  $\mathbf{s}(t) = (s_1(t), s_2(t), \dots, s_p(t))^T$ . Similarly, the intracellular metabolite concentrations of interest are denoted by a vector with dimension  $q$  at time  $t$  as  $\mathbf{\ell}(t) = (\ell_1(t), \ell_2(t), \dots, \ell_q(t))^T$ . Thus, at any time  $t$ , the state of extracellular and intracellular metabolite concentrations is denoted by

$$\mathbf{u}(t) = (\mathbf{s}(t)^T, \mathbf{\ell}(t)^T)^T.$$

To model the dynamic evolution of cell response to environmental perturbation during the iPSC culture process, at any time  $t$ , the specific reaction flux rates represented by a vector of with dimension  $n$  depend on the extracellular and intracellular metabolite concentrations, i.e.,

$$\mathbf{v}[\mathbf{u}(t)] = (v_1[\mathbf{u}(t)], v_2[\mathbf{u}(t)], \dots, v_n[\mathbf{u}(t)])^T.$$

Let  $N$  denote a  $(p + q) \times n$  stoichiometry matrix characterizing the structure of metabolic reaction network. Therefore, the dynamic evolution of extracellular and intracellular metabolite concentrations is modeled through a mass balance on the system of equations,

$$\frac{d\mathbf{u}(t)}{dt} = N\mathbf{v}[\mathbf{u}(t)]X(t). \quad (2)$$

**(2) Regulatory Mechanism Modeling and Learning.** To capture the cell response to environmental perturbation, a Michaelis–Menten (MM) formalism based regulation model was used to characterize the relationship of metabolic flux rates depending on the concentrations of associated substrates and inhibitors. This allows leveraging the existing biology knowledge and facilitating the learning of regulation mechanisms of iPSC metabolic reaction network from the experimental data.

Specifically, the  $g$ -th flux rate at the time  $t$  is modeled as,

$$v_g[\mathbf{u}(t)] = v_{max,g} \prod_{y \in \Omega_Y^g} \frac{u_y(t)}{u_y(t) + K_{m,y}} \prod_{z \in \Omega_Z^g} \frac{K_{i,z}}{u_z(t) + K_{i,z}}, \quad (3)$$

for  $g = 1, 2, \dots, n$ , where the set  $\Omega_Y^g$  represents the collection of activators (such as nutrients and substrates) influencing the flux rate  $v_g$  and the set  $\Omega_Z^g$  represents the collection of inhibitors dampening  $v_g$ . The parameters  $K_{i,\cdot}$ ,  $K_{m,\cdot}$ , and  $v_{max,\cdot}$  represent the affinity constant, the inhibition constant, and the maximum specific flux rate respectively. For iPSC cultures, the experimental data referenced were used to identify the critical activators and inhibitors, as well as learning the MM model coefficients.

**(3) Time-Course Isotopic Labeling Simulation.** Different <sup>13</sup>C-labeling patterns are generated by different flux distributions  $\mathbf{v}[\mathbf{u}(t)]$ . Thus, incorporating the dynamic system of isotopic labeling patterns (MID), which is a vector containing the fractional abundance of each mass state of metabolites, into the metabolic network kinetic model can aid in understanding intercellular metabolic network mechanisms. However, modeling each individual atom as one system state variable is computationally expensive. To address this issue, the elementary metabolite unit (EMU) framework was proposed, and it is based on a highly efficient decomposition method that can identify the minimum amount of information needed to simulate isotopic labeling<sup>23</sup>. Basically, the EMUs are created by using a decomposition algorithm and form the new basis for generating system equations that describe the relationship between fluxes and isotope measurements; see more detailed information in studies<sup>24,25,10,26,23,11,27</sup>.

Based on the study<sup>23,28</sup>, the reduced system can be obtained after decoupling based on EMUs with size  $r = 1, 2, \dots, R$  and connectivity. The time-dependent network was first identified: the decoupled EMUs with size  $r$  network,  $G_r(t) = \{V_r, E_r, W_r(t)\}$  with  $r = 1, 2, \dots, R$ . The vector  $V_r = (V_r^{(a)T}, V_r^{(b)T})^T$  is the set of vertices (i.e., EMUs) within the  $r$ -th network, the vector  $V_r^{(b)}$  with dimension  $|V_r^{(b)}|$  is the set of input EMUs (i.e., EMUs with size smaller than  $r$  or EMUs of extracellular carbon sources), the vector  $V_r^{(a)}$  with dimension  $|V_r^{(a)}|$  is the set of EMUs with size  $r$ .  $E_r$  is the adjacency matrix with dimension  $(|V_r^{(a)}| + |V_r^{(b)}|) \times (|V_r^{(a)}| + |V_r^{(b)}|)$  representing the dependence between each vertex. The corresponding weight matrix  $W_r(t)$  varies with time  $t$ . The non-negative  $(i, j)$ -th element  $W_r^{(i,j)}(t)$  indicates the flux rate of the reaction producing  $i$ -th EMU by consuming  $j$ -th EMU at time  $t$ .

Thus, at any time  $t$ , the dynamic isotopic labeling system can be defined as:

$$C_r'(t) = \frac{A_r(t) \cdot C_r(t) + B_r(t) \cdot D_r(t)}{P_r(t)} \quad (4)$$

where the rows of the state matrix  $C_r(t)$  correspond to the MIDs of EMUs within  $V_r^{(a)}$  at time  $t$ . The input matrix  $D_r(t)$  is analogous but with rows of input/carbon sources EMUs within  $V_r^{(b)}$  at time  $t$ . The concentration matrix  $P_r(t)$  is a diagonal matrix whose elements are pool sizes corresponding to EMUs represented in  $V_r^{(a)}$ . The construction of  $A_r(t)$  and  $B_r(t)$  are based on the decoupled EMU reaction network  $G_r(t)$ . The system matrix  $A_r(t)$  with size  $|V_r^{(a)}| \times |V_r^{(a)}|$  and matrix  $B_r(t)$  with size  $|V_r^{(a)}| \times |V_r^{(b)}|$  describe the metabolic network with elements defined as follows:

$$A_r^{(i,j)}(t) = \begin{cases} -\sum_{k=1}^{|V_r^{(a)}|} W_r^{(k,j)}(t), & i = j, \\ W_r^{(i,j)}(t), & i \neq j; \end{cases} \quad (5)$$

and

$$B_r^{(i,j)}(t) = W_r^{(i,|V_r^{(a)}|+j)}(t). \quad (6)$$

### 3.2 | iPSC Metabolic Reaction Network

The developed iPSC metabolic network model leverages central carbon metabolism from several previously published metabolic frameworks<sup>5,3,17,8,16,4</sup> and further learns from data. The iPSC metabolic network included glycolysis, TCA cycle, anaplerosis, PPP, and amino acid metabolism. For simplification, the reactions of PPP were collapsed into two reactions: Oxidative phase/branch and Non-oxidative phase/branch (i.e., No. 9 & 10 reaction in Table A1). During the exponential phase, greater than 90% of pentose-phosphate carbons is returned to glycolysis for the mammalian cell<sup>9,29</sup>. Thus, the synthesis of nucleotides and nucleic acids is considered an insignificant contributor to the model. The metabolic network is shown in Fig. 2 and the metabolic stoichiometry is listed in Table A1. The descriptions of metabolites and the enzymes conform to the Enzyme Commission Number (EC-No.) and are provided in Tables A3 and A4, respectively.

### 3.3 | Biokinetic Model of Flux Regulatory Mechanism

Due to the lack of energetic state and redox level measurements, each metabolic flux rate is modeled as dependent on the substrates and inhibitors concentrations using Michaelis–Menten model formalism. Similar to the existing studies<sup>5,3,17</sup>, for simplification purposes and also due to a lack of available data in the literature, a single affinity constant value is used for each metabolite. Additionally, reaction reversibility was considered during the iPSC culture model development for some key reactions. The final model is fully described in Table A2. Several regulatory mechanisms (i.e., No. **R1** to **R7**) are highlighted in Fig. 2, which were incorporated into the metabolic flux kinetics model to improve the model's prediction capability and better characterize the responses to environmental variations. These key final reactions are described below, where these new dependencies are highlighted in under brackets  $\underbrace{\dots\dots}$  with the corresponding regulatory mechanism No., while the original nomenclature is outside the brackets.

- Lactate accumulation has previously been reported to reduce glycolytic activity by inhibiting hexokinase (HK) and phosphofructokinase (PFK) activity in mammalian cells, where lactate acts as a signaling molecule to down-regulate PFK activity<sup>30,31,32</sup>. After evaluation of the experimental data, the model for HK was updated to

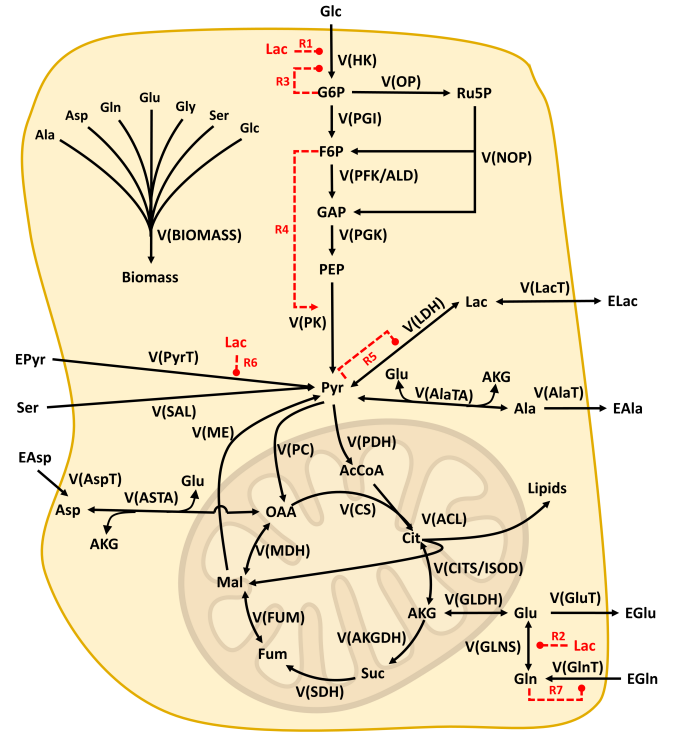


**FIGURE 2** The iPSC regulatory metabolic network. Glycolysis, PPP, TCA and anaplerosis and amino acid utilization are shown. Additionally, the regulatory mechanisms included in the dynamic model are shown. The metabolites descriptions are listed in Table A3. The enzyme description, including the Enzyme Commission Numbers (EC-No.) for each reaction, is listed in Table A4.

include this inhibitory effect of lactate on it:

$$v(HK) = v_{max,HK} \times \frac{Glc}{K_{m,Glc} + Glc} \times \underbrace{\frac{K_{i,LactoHK}}{K_{i,LactoHK} + Lac}}_{R1}. \quad (7)$$

- Since lactate inhibits glutaminase activity – the enzyme responsible for converting glutamine (GLN) to glutamate (GLU)<sup>33,34</sup> – the forward ( $f$ ) flux rate for the reaction, i.e.,  $Gln \leftrightarrow Glu + NH_4$ , was updated,

$$v(GLNSf) = v_{max,fGLNS} \times \frac{Gln}{K_{m,Gln} + Gln} \times \underbrace{\frac{K_{i,LactoGLNS}}{K_{i,LactoGLNS} + Lac}}_{R2}. \quad (8)$$

- Several regulatory functions, adapted from the studies<sup>16,15,17</sup>, were evaluated using the experimental data

to characterize activations and inhibitions. The regulatory mechanisms involved in glycolysis are described as: a) hexokinase inhibition by its product G6P, see **R3** in eq (9); b) activation of pyruvate kinase by F6P, see **R4** in eq (10), as well as c) the inhibition of lactate dehydrogenase reverse (*r*) reaction, see **R5** in eq (11), was changed to include the G6P inhibition:

$$v(HK) = v_{max,HK} \times \frac{Glc}{K_{m,Glc} + Glc} \times \frac{K_{i,LactoHK}}{K_{i,LactoHK} + Lac} \times \frac{K_{i,G6P}}{K_{i,G6P} + G6P}; \quad (9)$$

**R3**

$$v(PK) = v_{max,PK} \times \frac{PEP}{K_{m,PEP} \times \underbrace{\left[1 + \frac{K_{a,F6P}}{F6P}\right]}_{R4} + PEP}; \quad (10)$$

$$v(LDHr) = v_{max,rLDH} \times \frac{Lac}{K_{m,Lac} + Lac} \times \frac{K_{i,Pyr}}{K_{i,Pyr} + Pyr}. \quad (11)$$

**R5**

- Both lactate and pyruvate transport across the plasma membrane are facilitated by proton-linked monocarboxylate transporters (MCTs)<sup>29,35</sup>. More favorable lactate transport kinetics may decrease pyruvate consumption under high lactate culture conditions<sup>4,36</sup>. Thus, the model of PyrT was updated to:

$$v(PyrT) = v_{max,PyrT} \times \frac{EPyr}{K_{m,EPyr} + EPyr} \times \frac{K_{i,LactoPyr}}{K_{i,LactoPyr} + Lac}. \quad (12)$$

**R6**

- Since the transportation of extracellular-glutamine via cell membrane can be inhibited by intracellular-glutamine, the model for GlnT was updated to:

$$v(GlnT) = v_{max,GlnT} \times \frac{EGln}{K_{m,EGln} + EGln} \times \frac{K_{i,GLN}}{K_{i,GLN} + GLN}. \quad (13)$$

**R7**

### 3.4 | Model Fit and Goodness-of-fit Assessment

The proposed iPSC metabolic network kinetic model focuses on characterizing central carbon metabolism, including significant reactions from glycolysis, the TCA cycle, anaplerosis, PPP, and amino acid metabolism, along with regulatory mechanisms, across distinct cultural environments characterized by varying levels of glucose and lactate concentrations. The final model developed is shown in Table A1. This model includes 30 metabolic reactions with 32 variables (metabolites' concentration) in the reaction equations. The iPSC metabolic flux rate regulation biokinetic model, presented in Table A2, incorporates key activators and inhibitors for each reaction, dec their regulatory effects through the Michaelis–Menten model.

The proposed iPSC culture kinetic model estimates model parameters using the extracellular and MID data collected over time under the four different culture conditions. Denote the available extracellular metabolites concentrations data at time  $t$  as  $s_t^{meas}$  for  $t = 0, 12, 24, 36, 48$  hour. Denote intracellular isotopic labeling measurements at time  $t'$  as  $MID_{t'}^{meas}$  for  $t' = 24, 48$  hour. For the model fitting, the objective is minimizing the weighted sum of squared residuals (SSR) between available experimental data ( $s_t^{meas}, MID_{t'}^{meas}$ ) and model predicted values ( $s_t^{sim}, MID_{t'}^{sim}$ ),

$$\min \text{SSR} = \sum_{t=1}^T \frac{(s_t^{sim} - s_t^{meas})^2}{var_t^s} + \sum_{t'=1}^{T'} \frac{(MID_{t'}^{sim} - MID_{t'}^{meas})^2}{var_{t'}^M}, \quad (14)$$

where the weights are the inverse of the variances of the experimental measurements on extracllular metabolites and MIDs, i.e., ( $var_t^s, var_{t'}^M$ ). The fitting criteria in eq (14) allows the model to systematically and effectively fit the metabolic regulation network at different times.

The initial conditions for extracellular metabolites were obtained from culture data. As the experimental data only includes the relative abundance and the MIDs, estimates for the initial intracellular metabolite concentrations were sourced from the BRENDA Enzyme Database<sup>37</sup> and related references for mammalian cells cultured under similar conditions. Similarly, the initial kinetic parameter values were taken from the BRENDA Enzyme Database<sup>37</sup> and relevant references for similar metabolic networks and pathways.

The goodness-of-fit for the developed iPSC metabolic kinetic model was assessed based on predictions using a chi-square test. Basically, the null hypothesis is that the fitted model can faithfully represent the iPSC culture metabolic mechanism. This test assumes that the minimized variance-weighted SSR follows a chi-square distribution with  $d$  degrees of freedom, where the degree of freedom  $d$  equals the number of observations minus the number of fitted parameters. In this

study,  $p > 0.05$  indicates the model predictions are not significantly different than the measured values for the chi-square statistical test.

## 4 | RESULTS AND DISCUSSION

The simulator was estimated with limited experimental data and then validated in two manners. First, to mimic the dynamic data collection and assess the rolling forecasts required for process control, at any time  $t$ , the historical data were used to predict into the future. In Section 4.1, the model's ability to capture the dynamic evolution of iPSC metabolic characteristics was evaluated. The model was trained on experimental data collected over different time intervals (0-h to 12-h, 0-h to 24-h, and 0-h to 36-h), and used to predict the iPSC culture for up to 48-h. Second, to assess the model's ability to generalize and extrapolate to new conditions, three datasets, randomly selected from (1) high glucose and low lactate (HGLL); (2) high glucose and high lactate (HGHL); (3) low glucose and low lactate (LGLL); and (4) low glucose and high lactate (LGHL), were used to predict the fourth dataset with different initial conditions in Section 4.2. Basically, three of the conditions were used to train the model, then the fourth with different initial conditions was predicted. The four culture conditions were each examined in succession. Therefore, by validating the model's prediction performance under different experimental conditions, its robustness and usefulness for predicting iPSC characteristics in a variety of settings is verified.

### 4.1 | Prediction of iPSC Culture Process

During the model validation process, the proposed model simulator was trained using experimental data collected over various time intervals (0-h to 12-h, 0-h to 24-h, and 0-h to 36-h). The model's ability to predict the dynamic trajectories of key metabolites, including glucose, lactate, glutamate, glutamine, and pyruvate, as well as cell density, was evaluated by comparing the predicted values to experimental observations up to 48 hours. Fig. 3 provides a representative result of the cell culture process prediction for the case starting with HGLL. The results for the remaining settings, including HGHL, LGLL, and LGHL, are presented in Appendix Fig. B1 to B3.

The chi-square tests conducted on different time intervals were used to assess the goodness-of-fit of the predictive models. The prediction test statistics for the model trained on 0-12 hours of experimental data was 33.6 with 47 degrees of freedom ( $p$ -value = 0.93), while the test statistics for the model trained on 0-24 hours and 0-36 hours of experimental data were 82.6 with 107 degrees of freedom ( $p$ -value = 0.96) and 138.1

with 167 degrees of freedom ( $p$ -value = 0.95), respectively. All of the  $p$ -values are much greater than 0.05, which indicates the proposed metabolic kinetics simulator fits well with the experimental dataset. The results in Fig. 3 demonstrate that the fitted model can provide better predictions for most of the metabolite trajectories as more data are collected in time.

Overall, the predicted profiles of the iPSC cultures can closely track the dynamic patterns of the measured profiles and capture the cell culture dynamics. The experimental iPSC data were obtained from plates and dishes with limited space. Even though the overall growth rates were the same across the four conditions by experimental design, the growth rate decreased with time as nutrients were consumed and metabolic wastes accumulated. It is important to note that the developed mechanistic metabolic kinetic model is a simplified representation of the iPSC carbon central network, there could likely be some key metabolic regulations and biochemical reactions that were not incorporated; but they might be included for aggregate cultures. The less accurate predictive performances for lactate (under low lactate conditions) and glutamate may be due to the omission of key reactions or regulatory functions. For example, as suggested by the calibrated model in previous studies<sup>16,15,17</sup>, the membrane transportation of glutamate for mammalian cells is significantly impacted by the energetic state (ATP and ADP), and the forward and reverse conversion of lactate to pyruvate is influenced by the redox level (NAD and NADH).

Since the redox level and energetic state-related measurements were not collected for the iPSC cultures, these factors were not accounted for in the current model. The study<sup>18</sup> found for CHO cells, a redox parameter assisted with lactate predictions; however, the redox parameter implemented by this study was unmeasurable and thus would be difficult to incorporate into a control model. Furthermore, the lower prediction performance for glutamate may be attributed to its involvement in multiple reactions (see Fig. 2), leading to error accumulation over time. Future work should address these limitations with more comprehensive experimental data for iPSC cultures.

### 4.2 | Prediction across Different Initial Conditions

In order to understand how iPSC responds to different cultural conditions (i.e., variable glucose and lactate), cross validation was used, where one dataset is left out while training the model with data from the remaining three datasets. Fig. 4 shows the results of this cross training approach for the HGLL cultures where the HGHL, LGLL, and LGHL datasets were used. Cell density and key metabolites (i.e., glucose, lactate, glutamate, glutamine, and pyruvate) were predicted and are shown with the average of the measured values with standard deviations.

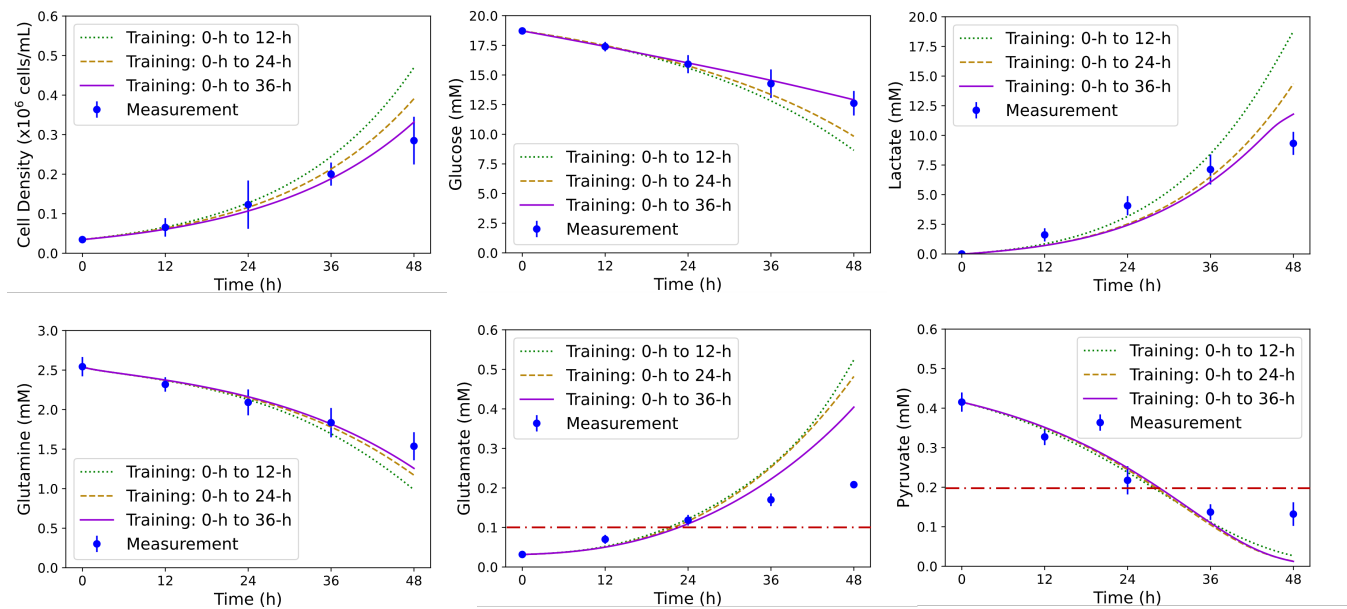


**FIGURE 3** Cell characteristic predictions for the high glucose and low lactate cultures using the dynamic model trained on different time intervals. (A) Cell density, (B) Glucose, (C) Lactate, (D) Glutamine, (E) Glutamate, and (F) Pyruvate. Times 0-h to 12-h (green dotted line); Times 0-h to 24-h (brown dashed line); and Times 0-h to 36-h (purple solid line). The detection limit of the Cedex Bioanalyzer is shown as the red dash-dot line.

The cross-condition extrapolation predictions for other culture conditions are provided in Appendix Fig. C4 to C6. To evaluate the goodness-of-fit, the chi-square test SSR statistics is 783 with 802 degrees of freedom with  $p$ -value = 0.67 much greater than 0.05. This  $p$ -value indicates that the metabolic kinetic model can faithfully represent the iPSC culture regulatory mechanisms under different levels of glucose and lactate concentrations.

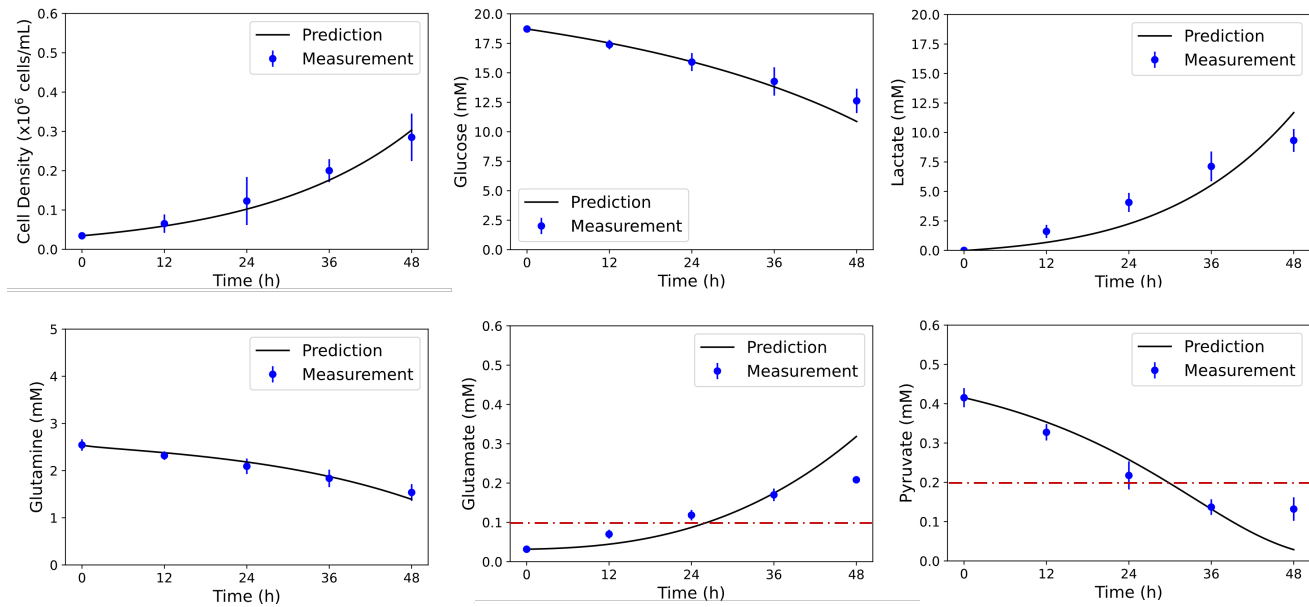
The predictions of intracellular MID from the  $[1,2-^{13}\text{C}_2]$  glucose and  $[\text{U}-^{13}\text{C}_3]$  glutamine tracer at 48-h under the control (HGLL) culture condition are shown in Fig. 5 and Fig. 6, respectively. Even though there is some prediction error, the simulation model can correctly predict the dynamics and interdependencies of multivariate iPSC culture process metabolism. The developed metabolic kinetic model can faithfully predict the cell response to environmental perturbation, which could guide the strategic feeding strategy for the integrated iPSC culture process for future research. In addition, by incorporating even the simplified PPP reactions, the M+1 isotopic labeling pattern for pyruvate and related metabolites from  $[1,2-^{13}\text{C}_2]$  glucose tracer can be well-predicted.

The prediction of metabolic flux maps for K3 iPSC under control culture at 24-h and 48-h are shown in Fig 7. The prediction performance of metabolic concentration trajectory and flux maps for K3 iPSC under HGHL, LGLL, and LGHL are provided in Appendix Fig. D7 to Fig. D9. Since no restrictive steady-state assumption was required for the developed

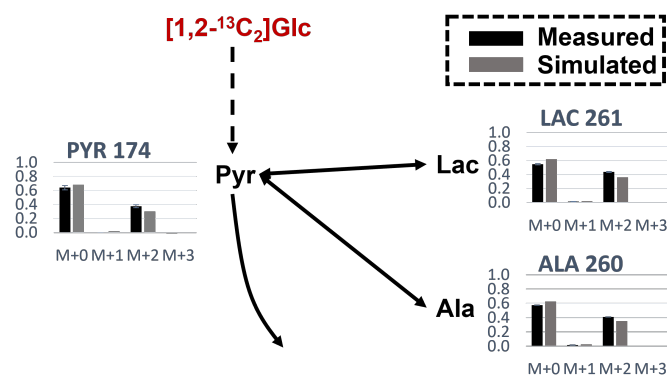
metabolic kinetic model, the flow-in flux is not required to be equal to the flow-out flux for each metabolite. Additionally, we observed a progressive rise in the flux rates of the TCA cycle as the iPSC culture process approaches the late exponential phase. This discovery is consistent with the observation reported in the literature study<sup>9</sup>.

Table 2 lists the prediction of consumption and production rates for the critical extracellular metabolites. The experimentally determined 12-h to 36-h biomass-specific uptake and production rates based on the Extracellular Time-Course Analysis (ETA) software<sup>38</sup> are also provided for comparison. Notice ETA results are based on metabolic steady-state assumption, which explains the reason that most ETA prediction of metabolites at 12-h to 36-h is located between the predictions of metabolites at 24-h and 48-h obtained by using the developed metabolic kinetic model. Under limited substrate conditions, the consumption rate changes significantly, as seen with glucose on LGLL and LGHL, and pyruvate on all four conditions. In contrast to methodologies based on the metabolic steady-state assumption, the proposed metabolic kinetic model captures these critical dynamic behaviors, which can facilitate the development of bioprocess control.

Moreover, the results presented in Table 2 are consistent with the regulatory mechanisms outlined in Section 3.3. Specifically, the consumption rate of glucose increases with higher extracellular glucose concentration (e.g., HGLL vs. LGLL and HGHL vs. LGHL), while it decreases with higher



**FIGURE 4** Cell characteristic predictions for the high glucose and low lactate cultures using the dynamic model trained on the other three case data sets. (A) Cell density, (B) Glucose, (C) Lactate, (D) Glutamine, (E) Glutamate, and (F) Pyruvate. The detection limit of the Cedex Bioanalyzer is shown as the red dash-dot line.



**FIGURE 5** MID pattern predictions from the  $[1,2-^{13}\text{C}_2]$  glucose tracer at 48-h for control (HGLL) cultures using the dynamic model trained on the other three data sets compared to literature measurements. MID patterns shown have been corrected for natural abundance.

extracellular lactate concentration (e.g., HGLL vs. HGHL and LGLL vs. LGHL), which is attributed to regulatory mechanism **R1** in eq (7). For lactate, the net production rate is lower when a certain amount of lactate exists in the cultural environment (see HGLL v.s. HGHL and LGLL v.s. LGHL). For pyruvate, in high lactate culture conditions, more favorable lactate transport kinetics of MCTs decreases pyruvate consumption (see HGLL v.s. HGHL and LGLL v.s. LGHL). This is associated with regulatory mechanism **R6** in eq (12).

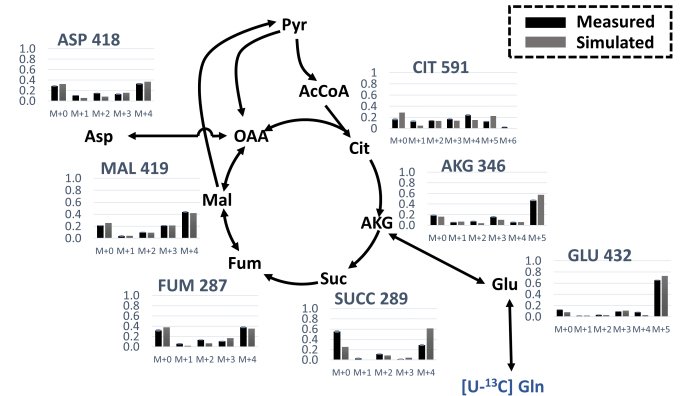


**FIGURE 6** MID pattern predictions from the  $[U-^{13}\text{C}_5]$  glutamine tracer at 48-h for control (HGLL) cultures using the dynamic model trained on the other three data sets compared to literature measurements. MID patterns shown have been corrected for natural abundance.

As the lactate dampens the conversion of glutamine to glutamate, under high lactate culture conditions, the consumption rate of glutamine and production rate of glutamate decrease (see HGLL v.s. HGHL and LGLL v.s. LGHL). This is associated with regulatory mechanisms **R2** in eq (8) and **R7** in eq (13). The ability of the proposed model to accurately predict dynamic cell behavior under environmental variations further confirms its reliability.

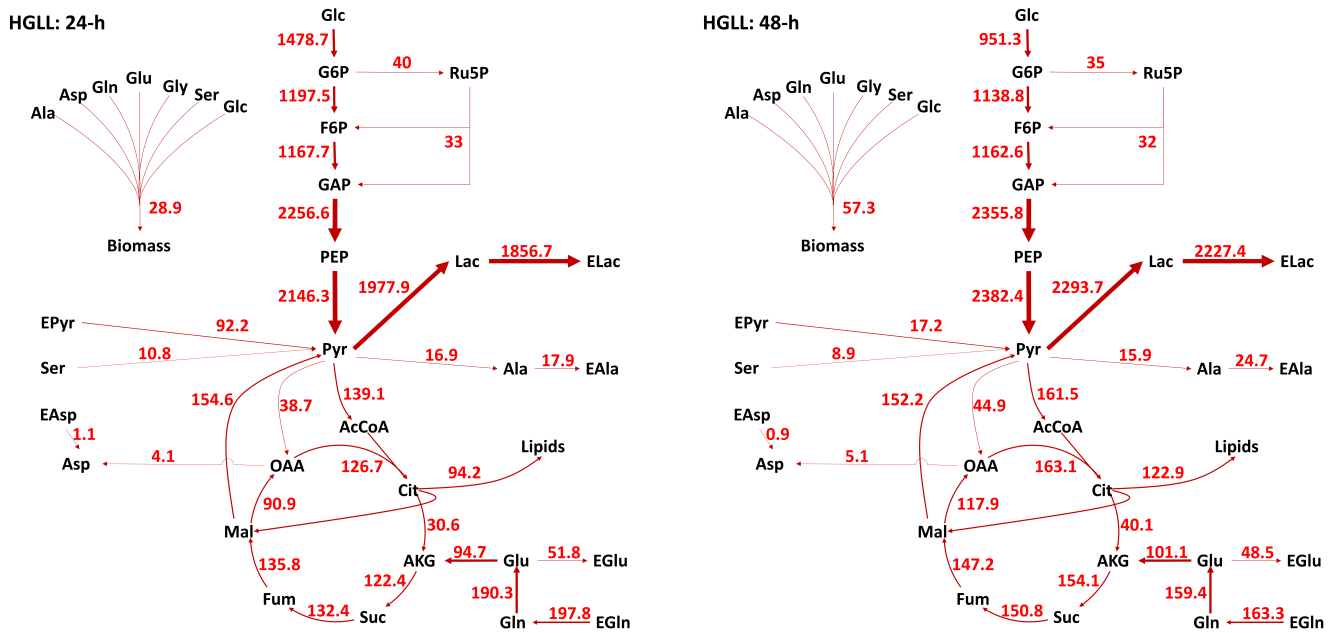


**FIGURE 7** Metabolic flux maps for K3 iPSC for the high glucose and low lactate cultures at 24-h and 48-h. Predicted fluxes are given in  $\text{nmol}/10^6$  cells-h. The line thicknesses represent the relative fluxes.

**TABLE 2** Dynamic model prediction for biomass-specific uptake and production rates for key extracellular metabolite ( $\text{nmol}/10^6$  cells-h). The fluxes obtained by Extracellular Time-Course Analysis (ETA) for 12-h to 36-h are calculated averages from measurements<sup>4</sup>, while the 24-h and 36-h fluxes predicted by the developed metabolic kinetic model are calculated for that specific time point. Negative values represent consumption rates and positive values represent production rates.

| Metabolite | HGLL ( $\text{nmol}/10^6$ cells-h) |         |                    | LGLL ( $\text{nmol}/10^6$ cells-h) |         |                    |
|------------|------------------------------------|---------|--------------------|------------------------------------|---------|--------------------|
|            | 24-h                               | 48-h    | 12-h to 36-h (ETA) | 24-h                               | 48-h    | 12-h to 36-h (ETA) |
| Glucose    | -1,478.7                           | -951.3  | -1,051             | -1,247.9                           | -255.3  | -994               |
| Lactate    | 1,856.7                            | 2,227.4 | 2,108              | 1,830.3                            | 1,701.3 | 2,000              |
| Pyruvate   | -92.1                              | -17.2   | -67.7              | -93.8                              | -18.5   | -75.2              |
| Glutamate  | 50.1                               | 48.5    | 36.2               | 51.3                               | 52.8    | 32.4               |
| Glutamine  | -197.8                             | -163.3  | -132               | -197.3                             | -160.4  | -147               |
| Metabolite | HGHL ( $\text{nmol}/10^6$ cells-h) |         |                    | LGHL ( $\text{nmol}/10^6$ cells-h) |         |                    |
|            | 24-h                               | 48-h    | 12-h to 36-h (ETA) | 24-h                               | 48-h    | 12-h to 36-h (ETA) |
| Glucose    | -828.9                             | -703.1  | -874               | -710.3                             | -493.6  | -860               |
| Lactate    | 1,522                              | 1,459.9 | 1,694              | 1,420                              | 1,119.7 | 1,651              |
| Pyruvate   | -65.2                              | -32.3   | -39                | -65.9                              | -33.9   | -36.5              |
| Glutamate  | 45.8                               | 44.1    | 28.3               | 46.4                               | 48.1    | 29.4               |
| Glutamine  | -175.2                             | -148.1  | -107               | -175.4                             | -148.1  | -120               |

## 5 | CONCLUSIONS

In this paper, we create a metabolic kinetic model characterizing the time-variate dynamics and regulatory mechanisms of the iPSC culture process. This model mainly focuses on central carbon metabolism, including glycolysis, TCA cycle, PPP,

anaplerosis, and key amino acid metabolism. The created iPSC metabolic regulatory network simulator is calibrated by using the experimental data on extracellular metabolite concentrations and intracellular isotopic measurements from multiple

tracers (i.e., [1,2-<sup>13</sup>C<sub>2</sub>] glucose, [U-<sup>13</sup>C<sub>5</sub>] glutamine and [U-<sup>13</sup>C<sub>3</sub>] sodium L-lactate tracers). These time-course measurements are collected heterogeneously at multiple time points along the cell culture process under different conditions (i.e., different levels of extracellular glucose and lactate concentrations). Both the capacities of iPSC culture process trajectory prediction under the same experimental initial condition and extrapolation across different initial conditions are assessed by using experimental measures. The developed metabolic kinetic model shows promising results and it provides a reliable prediction of stem cellular metabolic response to extracellular glucose and lactate concentration's perturbation. It can advance the understanding of the iPSC culture intracellular regulatory mechanisms, improve the capability for real-time cell culture process monitoring, and support optimal control for integrated iPSC culture processes.

## References

- Hanna E, Rémuzat C, Auquier P, Toumi M. Advanced therapy medicinal products: current and future perspectives. *Journal of market access & health policy* 2016; 4(1): 31036.
- Stephanopoulos G, Aristidou AA, Nielsen J. *Metabolic engineering: principles and methodologies*. 1998.
- Fiorenza S, Ritchie DS, Ramsey SD, Turtle CJ, Roth JA. Value and affordability of CAR T-cell therapy in the United States. *Bone marrow transplantation* 2020; 55(9): 1706–1715.
- Odenwelder DC, Lu X, Harcum SW. Induced pluripotent stem cells can utilize lactate as a metabolic substrate to support proliferation. *Biotechnology Progress* 2021; 37(2): e3090.
- Dressel R. Effects of histocompatibility and host immune responses on the tumorigenicity of pluripotent stem cells. In: . 33. Springer. ; 2011: 573.
- Kyriakopoulos S, Ang KS, Lakshmanan M, et al. Kinetic modeling of mammalian cell culture bioprocessing: the quest to advance biomanufacturing. *Biotechnology Journal* 2018; 13(3): 1700229.
- Wang LLW, Janes ME, Kumbhojkar N, et al. Cell therapies in the clinic. *Bioengineering & translational medicine* 2021; 6(2): e10214.
- Niklas J, Heinzle E. Metabolic flux analysis in systems biology of mammalian cells. *Genomics and Systems Biology of Mammalian Cell Culture* 2012: 109–132.
- Templeton N, Dean J, Reddy P, Young JD. Peak antibody production is associated with increased oxidative metabolism in an industrially relevant fed-batch CHO cell culture. *Biotechnology and bioengineering* 2013; 110(7): 2013–2024.
- Antoniewicz MR. Methods and advances in metabolic flux analysis: a mini-review. *Journal of Industrial Microbiology and Biotechnology* 2015; 42(3): 317–325.
- Antoniewicz MR. A guide to <sup>13</sup>C metabolic flux analysis for the cancer biologist. *Experimental & molecular medicine* 2018; 50(4): 1–13.
- Rivera-Ordaz A, Peli V, Manzini P, Barilani M, Lazzari L. Critical Analysis of cGMP Large-Scale Expansion Process in Bioreactors of Human Induced Pluripotent Stem Cells in the Framework of Quality by Design. *BioDrugs* 2021; 35(6): 693–714.
- Sengupta N, Rose ST, Morgan JA. Metabolic flux analysis of CHO cell metabolism in the late non-growth phase. *Biotechnology and bioengineering* 2011; 108(1): 82–92.
- Leighty RW, Antoniewicz MR. Dynamic metabolic flux analysis (DMFA): a framework for determining fluxes at metabolic non-steady state. *Metabolic engineering* 2011; 13(6): 745–755.
- Ghorbaniaghdam A, Chen J, Henry O, Jolicoeur M. Analyzing clonal variation of monoclonal antibody-producing CHO cell lines using an *in silico* metabolomic platform. *PLoS one* 2014; 9(3): e90832.
- Ghorbaniaghdam A, Henry O, Jolicoeur M. A kinetic-metabolic model based on cell energetic state: study of CHO cell behavior under Na-butyrate stimulation. *Bioprocess and biosystems engineering* 2013; 36: 469–487.
- Ghorbaniaghdam A, Henry O, Jolicoeur M. An *in-silico* study of the regulation of CHO cells glycolysis. *Journal of theoretical biology* 2014; 357: 112–122.
- Nolan RP, Lee K. Dynamic model of CHO cell metabolism. *Metabolic engineering* 2011; 13(1): 108–124.
- Borys BS, So T, Colter J, et al. Optimized serial expansion of human induced pluripotent stem cells using low-density inoculation to generate clinically relevant quantities in vertical-wheel bioreactors. *Stem Cells Translational Medicine* 2020; 9(9): 1036–1052.
- Meng G, Liu S, Poon A, Rancourt DE. Optimizing human induced pluripotent stem cell expansion in stirred-suspension culture. *Stem cells and development* 2017; 26(24): 1804–1817.

21. Kinney MA, Sargent CY, McDevitt TC. The multiparametric effects of hydrodynamic environments on stem cell culture. *Tissue Engineering Part B: Reviews* 2011; 17(4).
22. Nelson DL, Lehninger AL, Cox MM. *Lehninger principles of biochemistry*. Macmillan . 2008.
23. Antoniewicz MR, Kelleher JK, Stephanopoulos G. Elementary metabolite units (EMU): a novel framework for modeling isotopic distributions. *Metabolic engineering* 2007; 9(1): 68–86.
24. Ahn WS, Antoniewicz MR. Metabolic flux analysis of CHO cells at growth and non-growth phases using isotopic tracers and mass spectrometry. *Metabolic engineering* 2011; 13(5): 598–609.
25. Ahn WS, Antoniewicz MR. Parallel labeling experiments with [1, 2-<sup>13</sup>C] glucose and [U-<sup>13</sup>C] glutamine provide new insights into CHO cell metabolism. *Metabolic engineering* 2013; 15: 34–47.
26. Antoniewicz MR. A guide to metabolic flux analysis in metabolic engineering: Methods, tools and applications. *Metabolic engineering* 2021; 63: 2–12.
27. Jazmin LJ, Young JD. Isotopically nonstationary <sup>13</sup>C metabolic flux analysis. *Systems Metabolic Engineering: Methods and Protocols* 2013: 367–390.
28. Young JD, Walther JL, Antoniewicz MR, Yoo H, Stephanopoulos G. An elementary metabolite unit (EMU) based method of isotopically nonstationary flux analysis. *Biotechnology and bioengineering* 2008; 99(3): 686–699.
29. Halestrap AP. The monocarboxylate transporter family-structure and functional characterization. *IUBMB life* 2012; 64(1): 1–9.
30. Ivarsson M, Noh H, Morbidelli M, Soos M. Insights into pH-induced metabolic switch by flux balance analysis. *Biotechnology Progress* 2015; 31(2): 347–357.
31. Mulukutla BC, Gramer M, Hu WS. On metabolic shift to lactate consumption in fed-batch culture of mammalian cells. *Metabolic engineering* 2012; 14(2): 138–149.
32. Costa Leite T, Da Silva D, Guimarães Coelho R, Zancan P, Sola-Penna M. Lactate favours the dissociation of skeletal muscle 6-phosphofructo-1-kinase tetramers down-regulating the enzyme and muscle glycolysis. *Biochemical Journal* 2007; 408(1): 123–130.
33. Glacken M, Adema E, Sinskey A. Mathematical descriptions of hybridoma culture kinetics: I. Initial metabolic rates. *Biotechnology and bioengineering* 1988; 32(4): 491–506.
34. Hassell T, Gleave S, Butler M. Growth inhibition in animal cell culture: The effect of lactate and ammonia. *Applied biochemistry and biotechnology* 1991; 30: 29–41.
35. Huckabee WE. Control of concentration gradients of pyruvate and lactate across cell membranes in blood. *Journal of Applied Physiology* 1956; 9(2): 163–170.
36. Draoui N, Feron O. Lactate shuttles at a glance: from physiological paradigms to anti-cancer treatments. *Disease models & mechanisms* 2011; 4(6): 727–732.
37. Chang A, Jeske L, Ulbrich S, et al. BRENDA, the ELIXIR core data resource in 2021: new developments and updates. *Nucleic acids research* 2021; 49(D1): D498–D508.
38. Murphy TA, Young JD. ETA: robust software for determination of cell specific rates from extracellular time courses. *Biotechnology and bioengineering* 2013; 110(6): 1748–1758.



## **APPENDIX**

## A APPENDIX: TABLE

The following tables summarize detailed information about the constructed iPSC metabolic network and developed kinetic model.

- The iPSC metabolic network contains the major reactions for glycolysis, the TCA cycle, anaplerosis, PPP, and amino acid metabolism; see the specific reactions in Table A1 . The reactions of PPP are collapsed into two: Oxidative phase/branch and Non-oxidative phase/branch (i.e., No. 9 & 10 reactions).
- The iPSC metabolic flux rate regulation biokinetic model is summarized in Table A2 . Key activators and inhibitors are considered for each reaction, and their impact on the regulatory mechanisms is characterized through Michaelis–Menten model.
- The descriptions of the metabolites, considered in the developed metabolic kinetic model, are listed in Table A3 .
- For the developed metabolic kinetic model, the descriptions of the enzymes with Enzyme Commission Number (EC-No.) are provided in Table A4 . They are associated with metabolic flux reaction rates.

**TABLE A1** Reactions of the metabolic network

| No.                               | Pathway   |
|-----------------------------------|---|
| <b>Glycolysis</b>                 |   |
| 1                                 | Glc(abcdef) → G6P(abcdef)   |
| 2                                 | G6P(abcdef) → F6P(abcdef)   |
| 3                                 | F6P(abcdef) → GAP(cba) + GAP (def)  |
| 4                                 | GAP(abc) → PEP(abc)   |
| 5                                 | PEP(abc) → Pyr(abc)   |
| 6                                 | Pyr(abc) ↔ Lac(abc)   |
| 7                                 | EPyr(abc) → Pyr(abc)  |
| 8                                 | Lac(abc) ↔ ELac(abc)  |
| <b>PPP</b>                        |   |
| 9                                 | G6P(abcdef) → Ru5P(bcdef) + CO <sub>2</sub> (a)                                     |
| 10                                | Ru5P(abcde) + Ru5P(fghij) + Ru5P(klmno) → F6P(fgahij) + F6P(klbcd) + GAP(mno)       |
| <b>TCA</b>                        |   |
| 11                                | Pyr(abc) → AcCoA(bc) + CO <sub>2</sub> (a)  |
| 12                                | AcCoA(ab) + OAA(cdef) → Cit(fedbac)   |
| 13                                | Cit(abcdef) ↔ AKG(abcde) + CO <sub>2</sub> (f)                                      |
| 14                                | AKG(abcde) → Suc(bcde) + CO <sub>2</sub> (a)  |
| 15                                | Suc(abcd) → Fum(abcd)   |
| 16                                | Fum(abcd) ↔ Mal(abcd)   |
| 17                                | Mal(abcd) ↔ OAA(abcd)   |
| <b>Anaplerosis and Amino Acid</b> |   |
| 18                                | Mal(abcd) → Pyr(abc) + CO <sub>2</sub> (d)  |
| 19                                | Pyr(abc) + CO <sub>2</sub> (d) → OAA(abcd)  |
| 20                                | Gln(abcde) ↔ Glu(abcde) + NH <sub>4</sub>   |
| 21                                | Glu(abcde) ↔ AKG(abcde) + NH <sub>4</sub>   |
| 22                                | Glu(abcde) + Pyr(fgh) ↔ AKG(abcde) + Ala(fgh)                                       |
| 23                                | Ala(abc) → EAla(abc)  |
| 24                                | Glu(abcde) → EGlu(abcde)  |
| 25                                | EGln(abcde) → Gln(abcde)  |
| 26                                | Ser(abc) → Pyr(abc) + NH <sub>4</sub>   |
| 27                                | Asp(fghi) + AKG(abcde) ↔ Glu(abcde) + OAA(fghi) + NH <sub>4</sub>                   |
| 28                                | EAsp(abcd) → Asp(abcd)  |
| 29                                | Cit(abcdef) → Mal(fcba) + Lipids  |
| <b>Biomass</b>                    |   |
| 30                                | 0.19 Ala + 0.11 Asp + 0.1 Gln + 0.12 Glu + 0.17 Gly + 0.14 Ser + 0.16 Glc → Biomass |

**TABLE A2** Biokinetic equations of the metabolites fluxes (1-30) of the model

| No.               | Pathway   |
|-------------------|---|
| <b>Glycolysis</b> |   |
| 1                 | $v(HK) = v_{max,HK} \times \frac{Glc}{K_{m,Glc} + Glc} \times \frac{K_{i,G6P}}{K_{i,G6P} + G6P} \times \frac{K_{i,LactoHK}}{K_{i,LactoHK} + Lac}$ |
| 2                 | $v(PGI) = v_{max,PGI} \times \frac{G6P}{K_{m,G6P} + G6P}$   |
| 3                 | $v(PFK/ALD) = v_{max,PFK/ALD} \times \frac{F6P}{K_{m,F6P} + F6P}$   |
| 4                 | $v(PGK) = v_{max,PGK} \times \frac{GAP}{K_{m,GAP} + GAP}$   |
| 5                 | $v(PK) = v_{max,PK} \times \frac{PEP}{K_{m,PEP} \times (1 + \frac{K_{a,F6P}}{F6P}) + PEP}$  |
| 6f                | $v(LDHf) = v_{max,LDHf} \times \frac{Pyr}{K_{m,Pyr} + Pyr}$   |
| 6r                | $v(LDHr) = v_{max,LDHr} \times \frac{Lac}{K_{m,Lac} + Lac} \times \frac{K_{i,Pyr}}{K_{i,Pyr} + Pyr}$  |
| 7                 | $v(PyrT) = v_{max,PyrT} \times \frac{EPyr}{K_{m,EPyr} + EPyr} \times \frac{K_{i,LactoPyr}}{K_{i,LactoPyr} + Lac}$                                 |
| 8f                | $v(LacTf) = v_{max,LacTf} \times \frac{Lac}{K_{m,Lac} + Lac}$   |
| 8r                | $v(LacTr) = v_{max,LacTr} \times \frac{ELac}{K_{m,ELac} + ELac}$  |
| <b>PPP</b>        |   |
| 9                 | $v(OP) = v_{max,OP} \times \frac{G6P}{K_{m,G6P} + G6P}$   |
| 10                | $v(NOP) = v_{max,NOP} \times \frac{Ru5P}{K_{m,Ru5P} + Ru5P}$  |
| <b>TCA</b>        |   |
| 11                | $v(PDH) = v_{max,PDH} \times \frac{Pyr}{K_{m,Pyr} + Pyr}$   |
| 12                | $v(CS) = v_{max,CS} \times \frac{AcCoA}{K_{m,AcCoA} + AcCoA} \times \frac{OAA}{K_{m,OAA} + OAA}$  |
| 13f               | $v(CITS/ISODf) = v_{max,CITS/ISODf} \times \frac{Cit}{K_{m,Cit} + Cit}$   |
| 13r               | $v(CITS/ISODr) = v_{max,CITS/ISODr} \times \frac{AKG}{K_{m,AKG} + AKG}$   |
| 14                | $v(AKGDH) = v_{max,AKGDH} \times \frac{AKG}{K_{m,AKG} + AKG}$   |
| 15                | $v(SDH) = v_{max,SDH} \times \frac{Suc}{K_{m,Suc} + Suc}$   |
| 16f               | $v(FUMf) = v_{max,FUMf} \times \frac{Fum}{K_{m,Fum} + Fum}$   |
| 16r               | $v(FUMr) = v_{max,FUMr} \times \frac{Mal}{K_{m,Mal} + Mal}$   |
| 17f               | $v(MDHf) = v_{max,MDHf} \times \frac{Mal}{K_{m,Mal} + Mal}$   |
| 17r               | $v(MDHR) = v_{max,MDHR} \times \frac{OAA}{K_{m,OAA} + OAA}$   |

| <b>Anaplerosis and Amino Acid</b> |   |
|-----------------------------------|---|
| <b>18</b>                         | $v(ME) = v_{max,ME} \times \frac{Mal}{K_{m,Mal} + Mal}$   |
| <b>19</b>                         | $v(PC) = v_{max,PC} \times \frac{Pyr}{K_{m,Pyr} + Pyr}$   |
| <b>20f</b>                        | $v(GLNSf) = v_{max,fGLNS} \times \frac{Gln}{K_{m,Gln} + Gln} \times \frac{K_{i,LactoGLNS}}{K_{i,LactoGLNS} + Lac}$  |
| <b>20r</b>                        | $v(GLNSr) = v_{max,rGLNS} \times \frac{Glu}{K_{m,Glu} + Glu} \times \frac{NH_4}{K_{m,NH_4} + NH_4}$   |
| <b>21f</b>                        | $v(GLDHf) = v_{max,fGLDH} \times \frac{Glu}{K_{m,Glu} + Glu}$   |
| <b>21r</b>                        | $v(GLDHR) = v_{max,rGLDH} \times \frac{AKG}{K_{m,AKG} + AKG} \times \frac{NH_4}{K_{m,NH_4} + NH_4}$   |
| <b>22f</b>                        | $v(AlaTAf) = v_{max,fAlaTA} \times \frac{Glu}{K_{m,Glu} + Glu} \times \frac{Pyr}{K_{m,Pyr} + Pyr}$  |
| <b>22r</b>                        | $v(AlaTAr) = v_{max,rAlaTA} \times \frac{Ala}{K_{m,Ala} + Ala} \times \frac{AKG}{K_{m,AKG} + AKG} \times (1 + \frac{K_a,Gln}{Gln})$   |
| <b>23</b>                         | $v(AlaT) = v_{max,AlaT} \times \frac{Ala}{K_{m,Ala} + Ala}$   |
| <b>24</b>                         | $v(GluT) = v_{max,GluT} \times \frac{Glu}{K_{m,Glu} + Glu}$   |
| <b>25</b>                         | $v(GlnT) = v_{max,GlnT} \times \frac{EGln}{K_{m,EGln} + EGln} \times \frac{K_{i,GLN}}{K_{i,GLN} + GLN}$   |
| <b>26</b>                         | $v(SAL) = v_{max,SAL} \times \frac{Ser}{K_{m,Ser} + Ser}$   |
| <b>27f</b>                        | $v(ASTAf) = v_{max,fASTA} \times \frac{Asp}{K_{m,ASP} + Asp} \times \frac{AKG}{K_{m,AKG} + AKG}$  |
| <b>27r</b>                        | $v(ASTAr) = v_{max,rASTA} \times \frac{Glu}{K_{m,Glu} + Glu} \times \frac{OAA}{K_{m,OAA} + OAA} \times \frac{NH_4}{K_{m,NH_4} + NH_4}$  |
| <b>28</b>                         | $v(AspT) = v_{max,AspT} \times \frac{EAsp}{K_{m,EAsp} + EAsp}$  |
| <b>29</b>                         | $v(ACL) = v_{max,ACL} \times \frac{Cit}{K_{m,Cit} + Cit}$   |
| <b>Biomass</b>                    |   |
| <b>30</b>                         | $v(growth) = v_{max,growth} \times \frac{Gln}{K_{m,Gln} + Gln} \times \frac{Glc}{K_{m,Glc} + Glc} \times \frac{Glu}{K_{m,Glu} + Glu} \times \frac{Ala}{K_{m,Ala} + Ala} \times \frac{Asp}{K_{m,Asp} + Asp} \times \frac{Ser}{K_{m,Ser} + Ser} \times \frac{Gly}{K_{m,Gly} + Gly}$ |

**TABLE A3** Description of the Metabolite

| <b>Component</b> | <b>Description</b>         | <b>Component</b> | <b>Description</b>      |
|------------------|----------------------------|------------------|-------------------------|
| ACCoA            | Acetyl-CoezymeA            | ALA              | Alanine                 |
| AKG              | $\alpha$ -Ketoglutarate    | ASP              | Aspartate               |
| CIT              | Citrate                    | LAC              | Lactate                 |
| CO2              | Intracellular Carbonoxygen | GLN              | Glutamine               |
| F6P              | Fructose 6-Phosphate       | EGLY             | Extracellular Glycine   |
| G6P              | Glucose 6-Phosphate        | SER              | Extracellular Serine    |
| GAP              | Glyceraldehyde 3-Phosphate | GLC              | Extracellular Glucose   |
| GLU              | Glutamate                  | EGLN             | Extracellular Glutamine |
| GLY              | Glycine                    | EGLU             | Extracellular Glutamate |
| MAL              | Malate                     | EPYR             | Extracellular Pyruvate  |
| OAA              | Oxaloacetate               | EASP             | Extracellular Aspartate |
| PEP              | Phosphoenolpyruvate        | EALA             | Extracellular Alanine   |
| FUM              | Fumarate                   | ELAC             | Extracellular Lactate   |
| Ru5P             | Ribulose 5-Phosphate       | NH4              | Extracellular Ammonia   |
| SUC              | Succinate                  | LIPID            | Lipid                   |
| PYR              | Pyruvate                   | Bio              | Biomass                 |

**TABLE A4** Description of the Enzyme

| <b>Abbreviation</b> | <b>Description</b>                    | <b>EC-No.</b>     |
|---------------------|---------------------------------------|-------------------|
| HK                  | Hexokinase                            | 2.7.1.1           |
| PGI                 | Phosphoglucose Isomerase              | 5.3.1.9           |
| PFK/ALD             | Phosphofructokinase/Aldolase          | 2.7.1.11/4.1.2.13 |
| PGK                 | Phosphoglycerate Kinase               | 2.7.2.3           |
| PK                  | Pyruvate Kinase                       | 2.7.1.40          |
| OP                  | Oxidative Phase of PPP                |                   |
| NOP                 | Non-oxidative Phase of PPP            |                   |
| PyrT                | Membrane Transport of Pyruvate        |                   |
| SAL                 | Membrane Transport of Serine          |                   |
| LDH                 | Lactate Dehydrogenase                 | 1.1.1.27          |
| AlaTA               | Alanine Transaminase                  | 2.6.1.2           |
| PC                  | Pyruvate Carboxylase                  | 6.4.1.1           |
| PDH                 | Pyruvate Dehydrogenase                | 1.2.4.1           |
| CS                  | Citrate (Si)-Synthase                 | 2.3.3.1           |
| CITS/ISOD           | Aconitase/Isocitrate Dehydrogenase    | 4.2.1.3/1.1.1.41  |
| GLDH                | Glutamate Dehydrogenase               | 1.4.1.2           |
| GluT                | Membrane Transport of Glutamate       |                   |
| GLNS                | Glutamine Synthetase                  | 6.3.1.2           |
| AKGDH               | $\alpha$ -ketoglutarate Dehydrogenase | 1.2.1.105         |
| SDH                 | Succinate Dehydrogenase               | 1.3.5.1           |
| MDH                 | Malate Dehydrogenase                  | 1.1.1.37          |
| ME                  | Malic Enzyme                          | 1.1.1.40          |
| ASTA                | Aspartate Aminotransferase            | 2.6.1.1           |
| ACL                 | ATP citrate synthase                  | 2.3.3.8           |
| FUM                 | Fumarase                              | 4.2.1.2           |

## B APPENDIX: CELL CHARACTERISTIC PREDICTIONS

Fig. B1 to B3 depict the model prediction results of the iPSC culture process for three cases with different initial conditions, including high glucose and high lactate (HGHL), low glucose and low lactate (LGLL), and low glucose and high lactate cultures (LGHL) respectively.

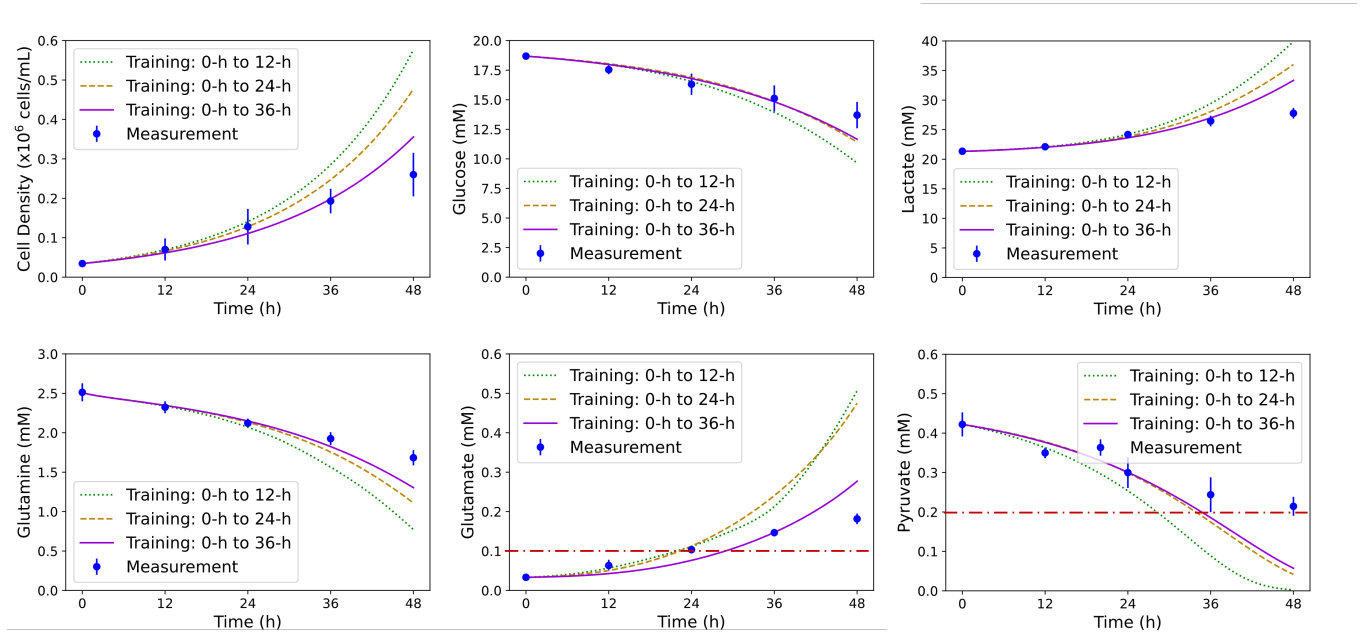


**FIGURE B1** Cell characteristic predictions for the high glucose and high lactate cultures using the dynamic model trained on different time intervals. (A) Cell density, (B) Glucose, (C) Lactate, (D) Glutamine, (E) Glutamate, and (F) Pyruvate. Times 0-h to 12-h (green dotted line); Times 0-h to 24-h (brown dashed line); and Times 0-h to 36-h (purple solid line). The detection limit of the Cedex Bioanalyzer is shown as the red dash-dot line.

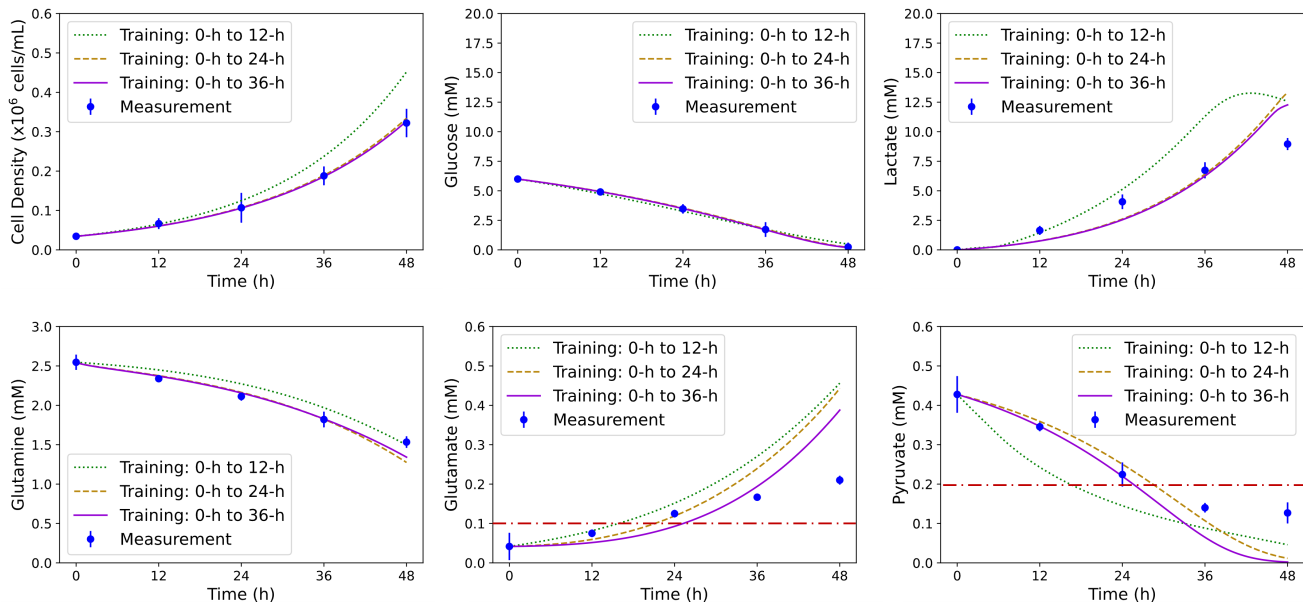


**FIGURE B2** Cell characteristic predictions for the low glucose and low lactate cultures using the dynamic model trained on different time intervals. (A) Cell density, (B) Glucose, (C) Lactate, (D) Glutamine, (E) Glutamate, and (F) Pyruvate. Times 0-h to 12-h (green dotted line); Times 0-h to 24-h (brown dashed line); and Times 0-h to 36-h (purple solid line). The detection limit of the Cedex Bioanalyzer is shown as the red dash-dot line.

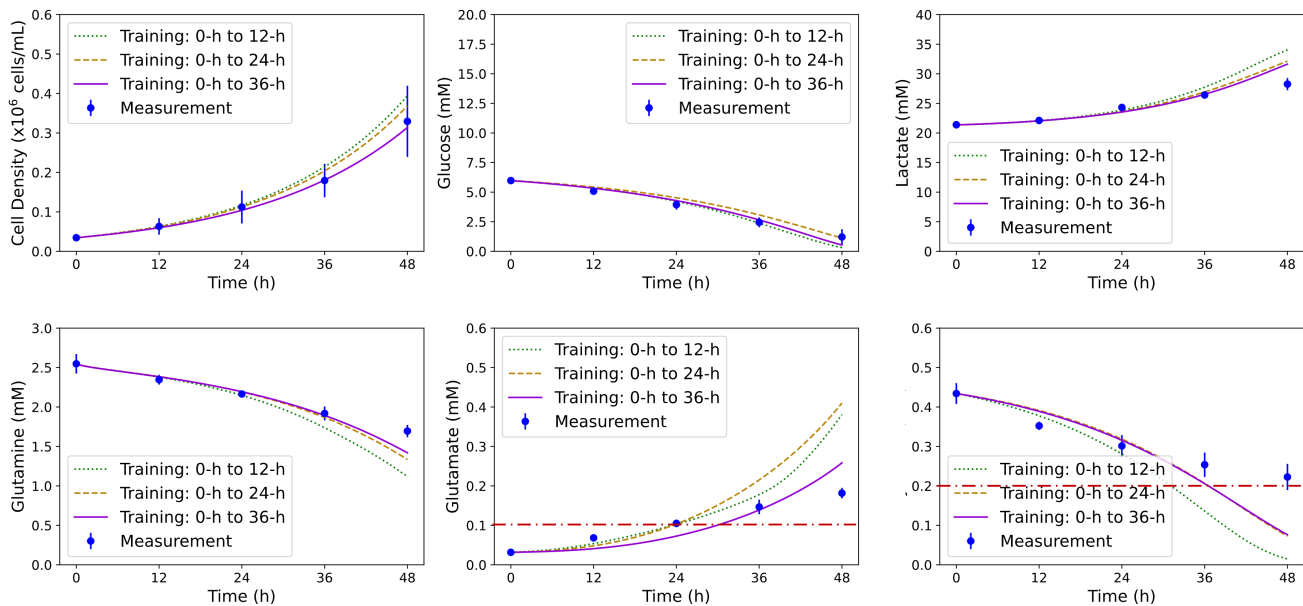


**FIGURE B3** Cell characteristic predictions for the low glucose and high lactate cultures using the dynamic model trained on different time intervals. (A) Cell density, (B) Glucose, (C) Lactate, (D) Glutamine, (E) Glutamate, and (F) Pyruvate. Times 0-h to 12-h (green dotted line); Times 0-h to 24-h (brown dashed line); and Times 0-h to 36-h (purple solid line). The detection limit of the Cedex Bioanalyzer is shown as the red dash-dot line.

## C APPENDIX: CELL CHARACTERISTIC ACROSS CULTURE CONDITION PREDICTIONS

Fig. C4 to C6 depict the prediction results across different initial conditions for cases, including high glucose and high lactate (HGHL), low glucose and low lactate (LGLL), and low glucose and high lactate (LGHL) respectively. Basically, the model is fitted by using the data from the remaining three cases.

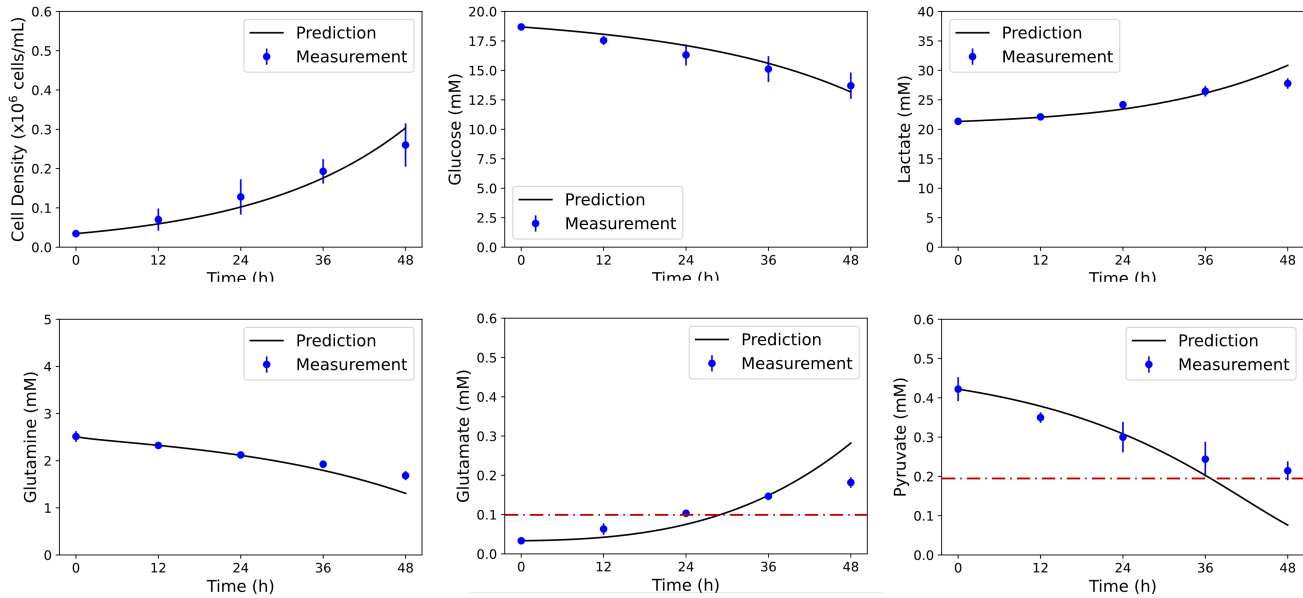


**FIGURE C4** Cell characteristic predictions for the high glucose and high lactate cultures using the dynamic model trained on the other three case data sets. (A) Cell density, (B) Glucose, (C) Lactate, (D) Glutamine, (E) Glutamate, and (F) Pyruvate. The detection limit of the Cedex Bioanalyzer is shown as the red dash-dot line.

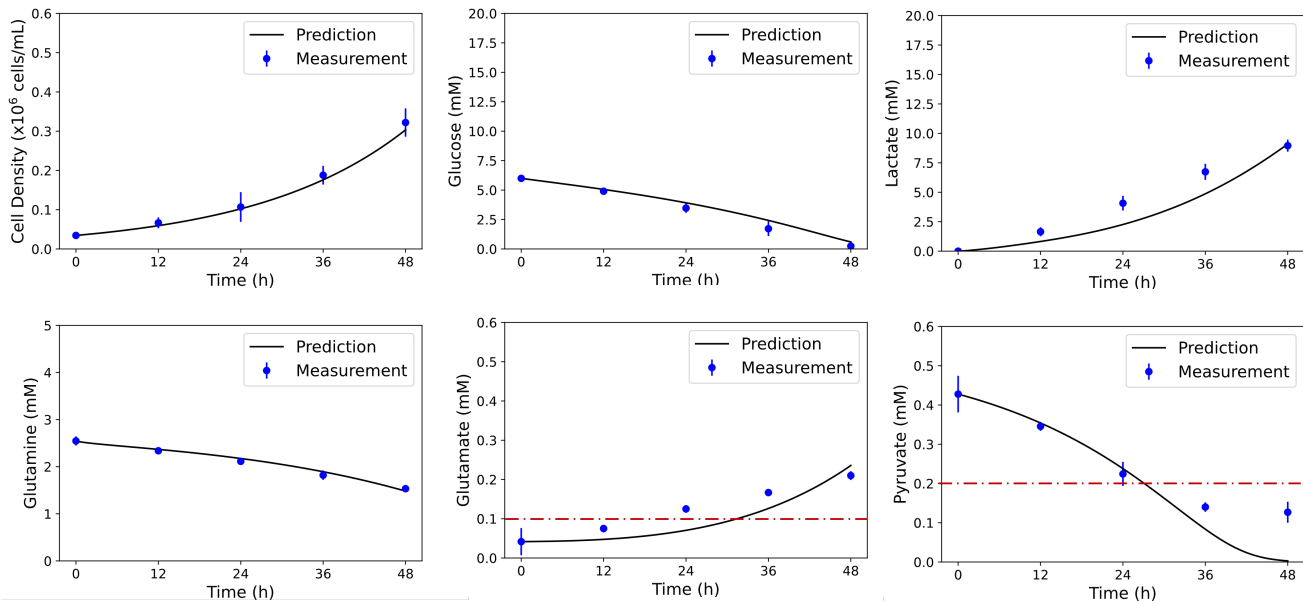


**FIGURE C5** Cell characteristic predictions for the low glucose and low lactate cultures using the dynamic model trained on the other three case data sets. (A) Cell density, (B) Glucose, (C) Lactate, (D) Glutamine, (E) Glutamate, and (F) Pyruvate. The detection limit of the Cedex Bioanalyzer is shown as the red dash-dot line.

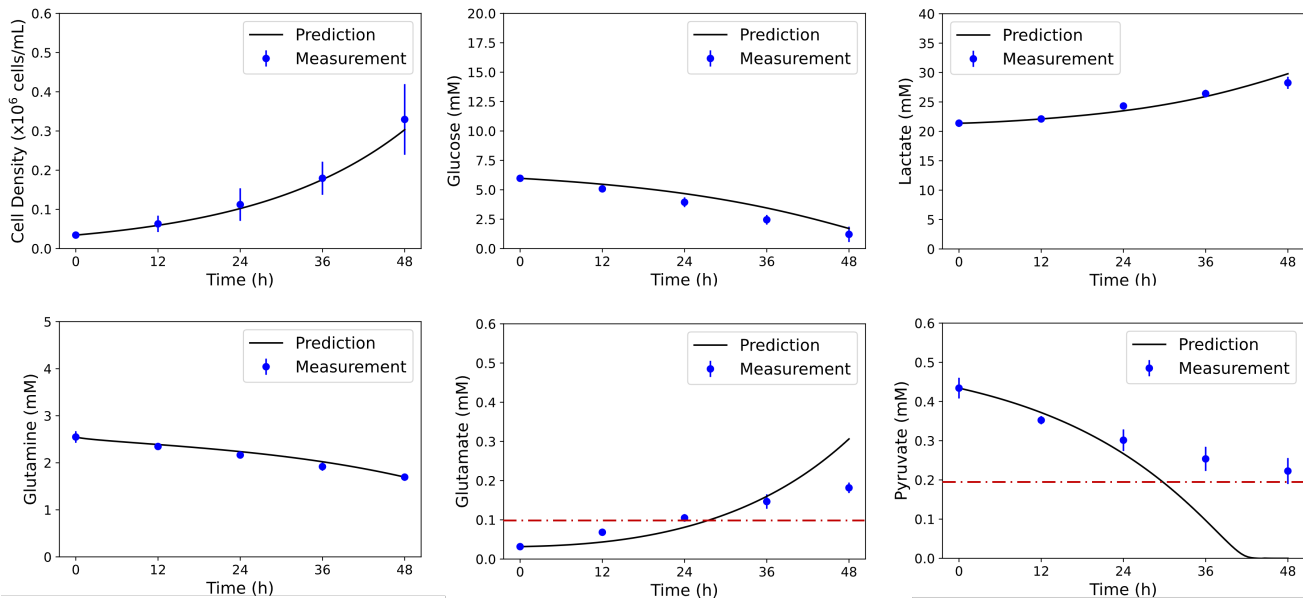


**FIGURE C6** Cell characteristic predictions for the low glucose and high lactate cultures using the dynamic model trained on the other three case data sets. (A) Cell density, (B) Glucose, (C) Lactate, (D) Glutamine, (E) Glutamate, and (F) Pyruvate. The detection limit of the Cedex Bioanalyzer is shown as the red dash-dot line.

## D APPENDIX: METABOLIC FLUX MAPS

Fig D7 to D9 depict the metabolic flux maps for iPSC culture at 24-h and 48-h respectively under the initial conditions, including high glucose and high lactate (HGHL), low glucose and low lactate (LGLL), and low glucose and high lactate (LGHL).

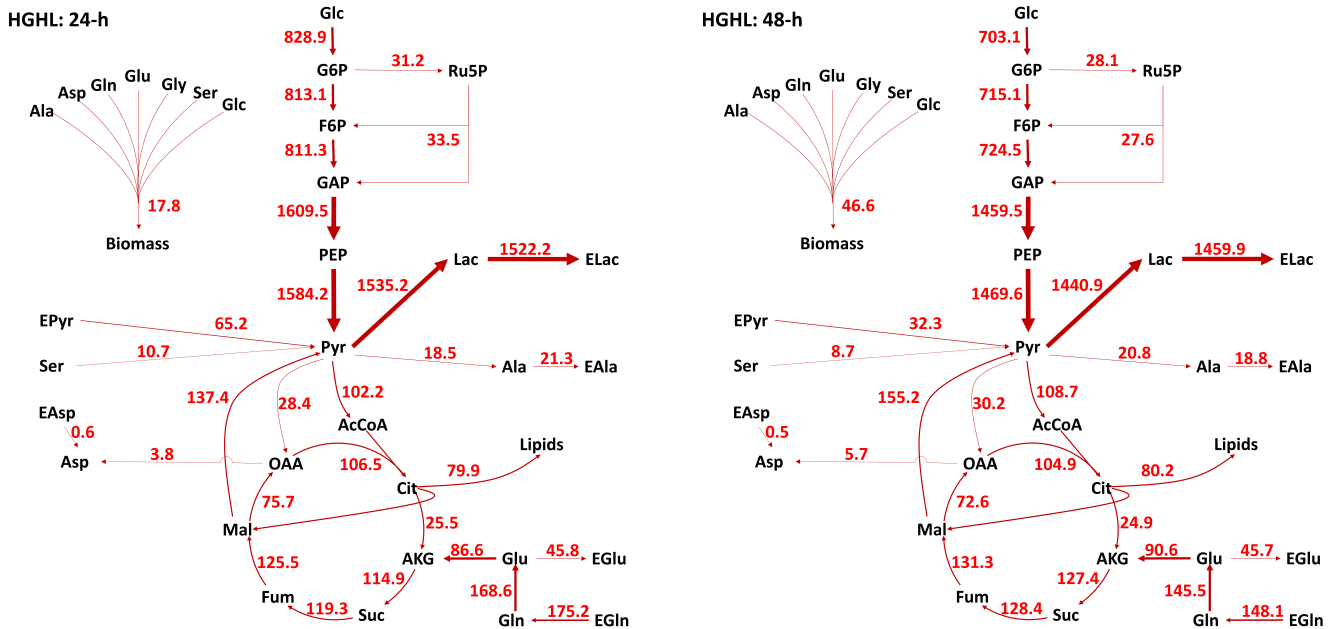


**FIGURE D7** Metabolic flux maps for K3 iPSC for the high glucose and high lactate cultures at 24-h and 48-h. Predicted fluxes are given in nmol/10<sup>6</sup> cells-h. The line thicknesses represent the relative fluxes.

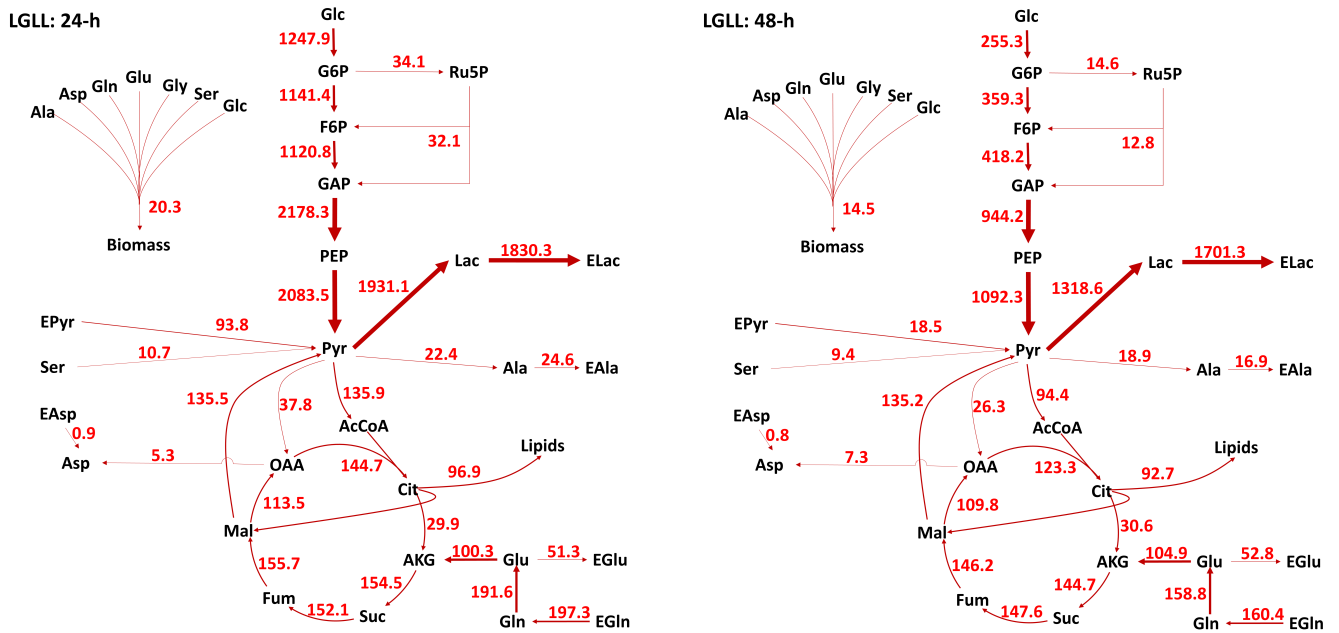


**FIGURE D8** Metabolic flux maps for K3 iPSC for the low glucose and low lactate cultures at 24-h and 48-h. Predicted fluxes are given in  $\text{nmol}/10^6$  cells·h. The line thicknesses represent the relative fluxes.

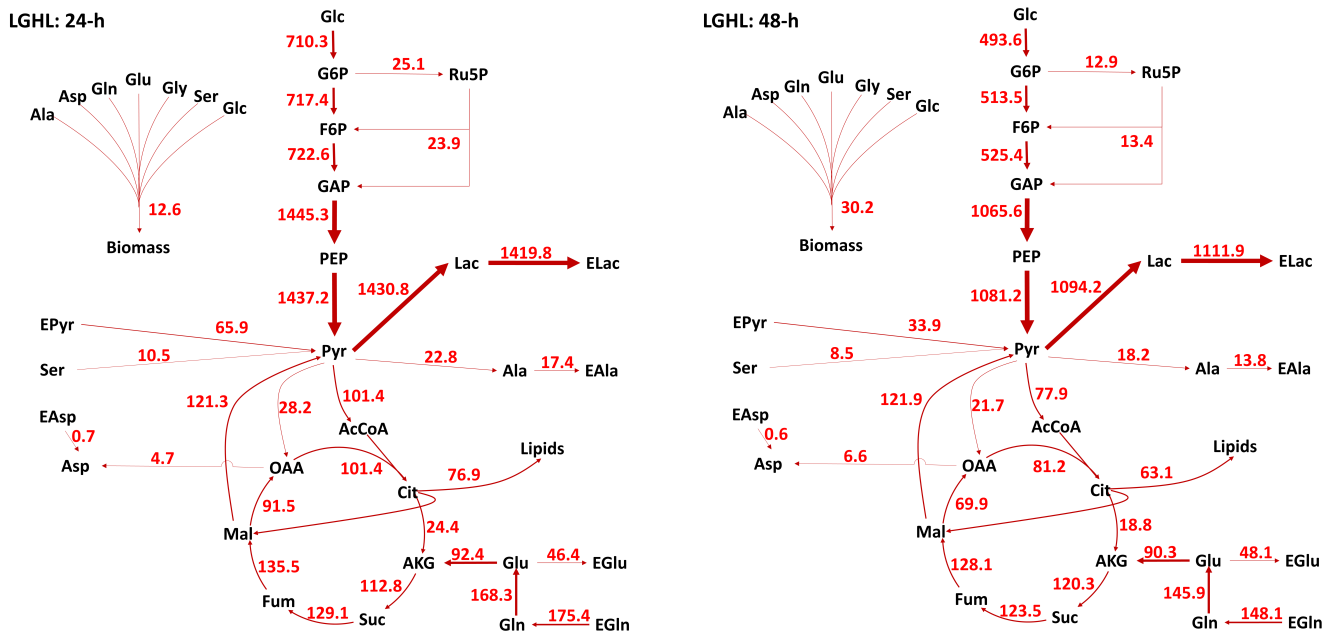


**FIGURE D9** Metabolic flux maps for K3 iPSC for the low glucose and high lactate cultures at 24-h and 48-h. Predicted fluxes are given in  $\text{nmol}/10^6$  cells·h. The line thicknesses represent the relative fluxes.